Effect of inertia on sheared disordered solids: Critical scaling of avalanches in two and three dimensions

K. Michael Salerno and Mark O. Robbins

Department of Physics and Astronomy, Johns Hopkins University, Baltimore, Maryland 21218, USA
(Received 10 September 2013; published 18 December 2013)

Molecular dynamics simulations with varying damping are used to examine the effects of inertia and spatial dimension on sheared disordered solids in the athermal quasistatic limit. In all cases the distribution of avalanche sizes follows a power law over at least three orders of magnitude in dissipated energy or stress drop. Scaling exponents are determined using finite-size scaling for systems with 10^3–10^6 particles. Three distinct universality classes are identified corresponding to overdamped and underdamped limits, as well as a crossover damping that separates the two regimes. For each universality class, the exponent describing the avalanche distributions is the same in two and three dimensions. The spatial extent of plastic deformation is proportional to the energy dissipated in an avalanche. Both rise much more rapidly with system size in the underdamped limit where inertia is important. Inertia also lowers the mean energy of configurations sampled by the system and leads to an excess of large events like that seen in earthquake distributions for individual faults. The distribution of stress values during shear narrows to zero with increasing system size and may provide useful information about the size of elemental events in experimental systems. For overdamped and crossover systems the stress variation scales inversely with the square root of the system size. For underdamped systems the variation is determined by the size of the largest events.

I. INTRODUCTION

Many slowly driven systems respond to a driving force through bursts of activity termed avalanches. These avalanches often follow a power-law distribution over many decades, signaling the existence of a nonequilibrium critical depinning transition at the onset of motion. Systems showing this scaling behavior include charge-density waves, fluid interfaces, magnetic domain walls, granular media, foams, crystals, amorphous metals, and the earth's crust [1–10].

One of the unresolved aspects of the depinning transition is the role of inertia. Most computational work has focused on the overdamped limit and studies that include inertia suggest that it fundamentally changes the depinning transition from a continuous second-order transition to a discontinuous transition with hysteresis [11–14]. In contrast, experiments have reported power-law scaling even in systems that display underdamped dynamics such as earthquakes and compressed laboratory samples. In this paper we present simulations of quasistatic plastic deformation in two- and three-dimensional disordered solids that show that inertia does not destroy critical behavior at depinning, but does change the universality class.

Theoretical studies of avalanches have generally considered lattice-based models with simple site interaction rules [8–23]. These models are computationally and analytically tractable, but have the limitation that position and stress changes are discrete. Most studies consider scalar order parameters, ignore correlations in deformation, and are in the overdamped limit. Then the rate of avalanches of size S follows a power law $R(S) \sim S^{-\tau}$, with a universal value of $\tau = 3/2$ [16,17]. Strain and stress in deformed solids are tensorial quantities rather than scalars. A recent model shows that this can produce a lower value of $\tau = 1.25$ [21] and produce long-range spatial correlations in deformation like those found in atomistic simulations [24]. Older models with different rules for site evolution, such as long-term damage to sites, also find

that spatial correlations affect the power-law exponents for avalanche statistics [9].

Another limitation of lattice models is the difficulty of including inertia. One common approach is to add rules that lower barriers to motion when an avalanche starts [10,13–16]. This fits the intuitive picture that inertia can carry a system over successive potential energy barriers, but inertia is highly directional and decreases the chance of passing over barriers that are not in the direction of the momentum. Studies of scalar lattice models find that including inertia in this simple way fundamentally changes the nature of the depinning transition. All find that inertia introduces hysteresis, with different stresses required to initiate and stop motion [13–15,25]. Most predict that the transition becomes first order [13,14,25], but a hysteretic second order has also been proposed [15]. Experimental evidence for hysteresis and a first-order depinning transition has been reported for granular media and sandpiles [26,27].

Many other experiments have reported a continuous second-order transition with critical scaling in plastically deformed disordered solids, including granular packings, colloidal glasses, foams, and metallic glasses [28–37]. The longest range of scaling is for earthquakes, where the conversion of the magnitude on the Richter scale to the energy or moment is complicated, but gives $\tau = 5/3$ [38]. Studies of granular media have found values of τ that are 2–6 [31,37] or as small as 1.2 [7,37,39]. Sun *et al.* have reported results from deformation of bulk metallic glasses, finding avalanche distribution exponents τ between 1.3 and 1.5 [40,41]. The variation in laboratory measurements reflects the difficulty in detecting events with a wide range of sizes. In addition, it is difficult to vary the rate, system size, and other experimental parameters that cut off the largest events and influence the apparent exponent [10]. Simulations allow a full analysis of these effects.

Particle-based simulations of plastic deformation provide more realistic microscopic detail than lattice models, but are also computationally more intensive. Early simulations of bubbles in the overdamped limit found a power-law distribution of rearrangements with exponent $\tau = 0.7$ [42,43]. Maloney and Lemaître found similar scaling using energy-minimization dynamics for quasistatic shear of a model two-dimensional glass, but τ appeared to decrease from 0.7 to 0.5 with increasing system size [44]. They also found that the size of the largest avalanche increased with system size, as expected at a critical depinning transition. A power-law increase in event size was seen in later simulations of a similar two-dimensional model by Lerner and Procaccia [45] and three-dimensional simulations of a more realistic model of amorphous metals by Bailey *et al.* [46]. The computational studies described above have all been on systems of about 2×10^4 particles or less, restricting the range of power-law scaling and making τ difficult to measure.

In a recent paper [47], we examined scaling of avalanches in two-dimensional systems with more than 10^6 particles. This allowed τ and other critical exponents to be determined as a function of damping. The results showed that the depinning transition remained second order in the underdamped limit, but that the universality class changed with damping. The current paper expands our studies of two-dimensional systems and extends them to three dimensions. All simulations are performed in the athermal quasistatic limit, but with varying levels of damping to change the role of inertia in the system. Finite-size scaling is used to develop scaling relations between critical exponents and analyze data from systems with the number of particles ranging from thousands to several million.

We find that inertia leads to the same three universality classes in two and three dimensions. Some of the exponents, including τ, are independent of dimension. In the overdamped limit, τ is close to the value of 1.25 obtained in a recent lattice model that includes directional stress transfer [21] and less than the value of 1.5 obtained for scalar lattice models [10,14,16]. In the underdamped limit, τ is also near 1.25, but the distribution of stress drops can exhibit a higher apparent exponent. The most dramatic effect of inertia is to increase the prevalence of large avalanches. The magnitude of the largest events grows more rapidly with system size and the avalanche distribution has a plateau at large magnitudes. The longest range of scaling is observed for the crossover damping that corresponds to a multicritical point separating the overdamped and underdamped regimes. The energy scales with $\tau = 1$ for more than five decades.

There is no evidence of the hysteresis predicted by lattice models of inertia [11,12,14–16,25]. The range of stresses sampled during quasistatic motion shrinks to zero with increasing system size. In the overdamped limit, stress fluctuations decrease as the inverse square root of the number of particles. Stress fluctuations drop more slowly in the underdamped limit, where they are determined by the size of the largest avalanches. In all cases, the rise in maximum avalanche size with system size reduces the rate of small avalanches, which scales sublinearly with system size. Both effects may be useful in analyzing the effective size of elemental deformations in experimental systems.

The relationship between the change in shear stress, energy dissipation, and plastic deformation during individual avalanches is studied in detail. The drop in stress and the energy dissipated are uncorrelated for small events, but become linearly related for the larger events that exhibit critical scaling. The spatial size of avalanches is proportional to the energy dissipated. This provides evidence that bigger avalanches spread over a larger area rather than producing greater local strains in the deformed region.

An outline of the remainder of the paper is as follows. Section II details the system studied, including the particle interactions, damping, and protocol for reaching the quasistatic limit in simulations with inertia. Section III presents results for the effect of inertia on the energies and stresses sampled during shear, the rate of avalanches, the critical scaling exponents, and the relation between the energy dissipated, stress change, and plastic deformation associated with each avalanche. Finally, Sec. IV presents a discussion and summary of the findings.

II. METHODS

This paper presents results from molecular dynamics (MD) simulations of deformed disordered solids in two and three dimensions. In all cases, the system studied is a binary glass. The two species of particles A and B both have mass m, but have different diameters to prevent crystallization. The particles interact via a smoothed Lennard-Jones (LJ) potential, which depends only on the magnitude r of the vector $\mathbf{r}$ between two particles and their species. This potential keeps the standard LJ form at small distances

$$U_{IJ}(\mathbf{r}) = 4u[(a_{IJ}/r)^{12} - (a_{IJ}/r)^6] + u_c, \quad r < 1.2a_{IJ}, \quad (1)$$

where u is the characteristic energy, u_c is an energy offset, and a_{IJ} is the interaction length between particles of type I and J. The A-A particle interaction length is taken as the fundamental unit of length $a \equiv a_{AA}$. The B-B particle interaction length $a_{BB} = 3/5a$, while the mixed interaction length $a_{AB} = a_{BA} = 4/5a$. Outside the LJ region the potential has a polynomial form

$$U_{IJ}(\mathbf{r}) = C_1\left(r - r_{IJ}^{(c)}\right) + \frac{C_2}{2}\left(r - r_{IJ}^{(c)}\right)^2 + \frac{C_3}{3}\left(r - r_{IJ}^{(c)}\right)^3$$
$$+ \frac{C_4}{4}\left(r - r_{IJ}^{(c)}\right)^4, \quad 1.2a_{IJ} < r < 1.5a_{IJ}, \quad (2)$$

with coefficients C_i chosen so that the energy, the force, and the derivative of the force match the LJ form at the inner cutoff radius $1.2a_{IJ}$ and go to zero at an outer cutoff radius $r_{IJ}^{(c)} = 1.5a_{IJ}$. For these cutoff radii the binding energy of a single bond is about $0.5u$. The strength of the interaction, particle radius, and mass set the fundamental unit of time $t_0 = \sqrt{ma^2/u}$. Simulations were performed with the LAMMPS MD simulation code, using a velocity Verlet integration algorithm with an integration time step $\Delta t = t_0/200$ [48].

Two-dimensional systems are initialized by placing particles at random in a square periodic simulation cell with the ratio of the number of particles of species A and B: $N_A/N_B = (1 + \sqrt{5})/4$. Next, the system is heated well above the glass transition temperature and then quenched to zero temperature at constant pressure. The pressure is chosen to be near zero, but slightly compressive. The results are insensitive to the

precise value. Following this procedure, the system density is $\rho = 1.38a^{-2}$ and the square simulation box has period L. We consider five box sizes with $L = 55a, 109a, 219a, 437a,$ and $875a$. These sizes correspond to $N \approx 4 \times 10^3$ to 10^6 particles.

A similar equilibration protocol is followed for three dimensions. After equilibration the density is $\rho = 1.71a^{-3}$ and the simulation is a cube with period L. Sizes are $L = 20a, 40a,$ and $81a$, corresponding to $N \approx 10^4$–10^6 particles.

After the quench process, the samples are strained. The periodic boundary conditions are changed and a corresponding affine displacement is applied to the position of each particle. The deformation applied to the simulation box in two dimensions is a pure shear strain at a true strain rate $\dot\epsilon = \dot\epsilon_{xx} = -\dot\epsilon_{yy}$. In three dimensions the system volume is conserved by applying an axisymmetric compressive strain rate $-\dot\epsilon$ in two dimensions x and y and an extensional strain rate $2\dot\epsilon$ in the third direction z. The deformation leads to changes in the instantaneous stress tensor, which is calculated from the kinetic energy tensor and the virial tensor for all particles [49].

Our aim is to study the athermal limit, which requires constantly removing kinetic energy from the simulation. A viscous drag force is applied to damp particle motion. The drag force has the form $\mathbf{F}_{\text{drag}} = -\Gamma m \mathbf{v}$, where $\mathbf{v}$ is the peculiar velocity, with displacement due to the affine deformation subtracted. The dissipation rate Γ plays a central role in our simulations by controlling the relative importance of the inertial term in the particle equations of motion. As Γ decreases, the dynamics changes from overdamped to underdamped (inertial) dynamics.

Generically, a strained disordered solid will load elastically for some strain interval and then plastically deform, decreasing the stress in the system and releasing stored elastic energy as kinetic energy. These sudden bursts of particle motion are termed avalanches. In the quasistatic limit the series of elastic loading segments and plastic deforming avalanche events should be independent of the strain rate and depend only on the total strain interval. One way to realize this limit is to deform the system at a very low rate so that the kinetic energy from one avalanche has been dissipated long before the system has been strained enough to nucleate the next avalanche. Since the rate must be set low enough to prevent overlap of the closest events, this is not computationally feasible for all system sizes and damping rates. Instead, we implement a protocol where the system is strained at a finite strain rate, which is then reduced to zero when an avalanche is detected.

A representative strain-avalanche-strain interval, shown in Fig. 1, illustrates how the system evolves with this quasistatic avalanche detection scheme. When the system is deformed, the nonaffine response due to heterogeneity in the solid produces a small background kinetic energy density $\mathcal{K}_{\text{back}}$. This kinetic energy is nearly constant during elastic loading at constant strain rate (solid lines). When an avalanche starts, there is a sharp rise in kinetic energy. The strain rate is reduced to zero when the kinetic energy exceeds $\mathcal{K}_{\text{back}}$ by roughly two orders of magnitude. The straining of the solid resumes when the kinetic energy has fallen below $\mathcal{K}_{\text{back}}$ by at least two orders of magnitude. We have checked that the strain rate
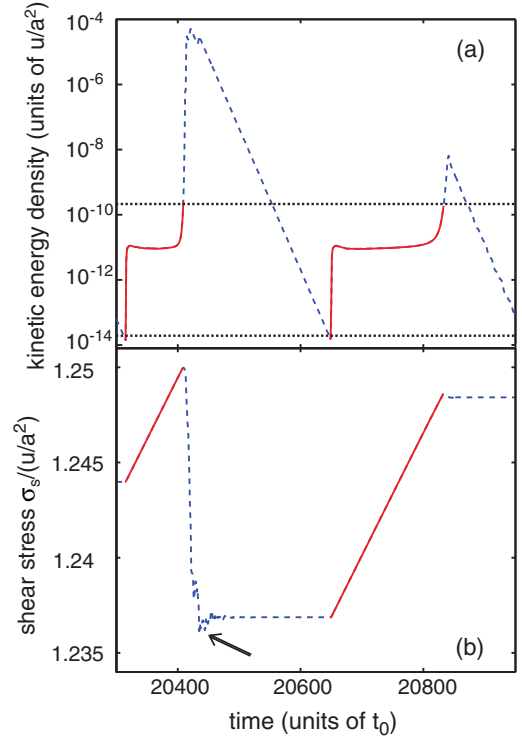

FIG. 1. (Color online) (a) Event sequence showing the kinetic energy thresholds (dotted horizontal lines) used to reach the quasistatic limit. Here an $L = 219a$ system is strained at a rate of $\dot\epsilon = 10^{-6} t_0^{-1}$ during the solid (red) segments. The plateaus of low constant kinetic energy $\mathcal{K}_{\text{back}}$ result from nonaffine displacements due to heterogeneity. Avalanches cause a sharp spike in kinetic energy that decays more rapidly as Γ increases. The strain rate is set to zero (dashed blue segments) after the upper threshold is exceeded and returned to $10^{-6} t_0^{-1}$ when a lower threshold is passed. (b) The stress-strain curve rises linearly during elastic loading (solid red segments) and drops rapidly as the avalanche begins (dashed blue segments). There is often an overshoot (arrow) where the stress drops below the steady-state value.

chosen is low enough that the results are not sensitive to these thresholds.

The stress response of the system illustrated in Fig. 1(b) is typical, showing linear behavior during the strain interval, followed by a rapid drop during an avalanche event. During avalanches with low particle damping the stress often overshoots the steady-state value that is used to quantify the size of avalanches. This overshoot complicates the analysis of simulations at constant strain rate.

Even after eliminating the connection between strain rate and avalanche duration, there is still the problem of the very long duration of large avalanches at very low damping rates. As the damping coefficient Γ becomes small and events become large, the peak kinetic energy in the system approaches $10^{-3} u$ per unit area (volume). At our prescribed strain rates there is then a factor of $\mathcal{K}_{\text{max}}/\mathcal{K}_{\text{back}} \approx 10^8$ between the maximum kinetic energy and the kinetic energy during straining. This energy must be removed by the viscous drag force and one can estimate that for the smallest damping rates we simulate, $\Gamma t_0 = 10^{-3}$, the decay of the kinetic energy will take a time of about $\ln(\mathcal{K}_{\text{max}}/\mathcal{K}_{\text{back}})/\Gamma \approx 20\,000 t_0$. This is
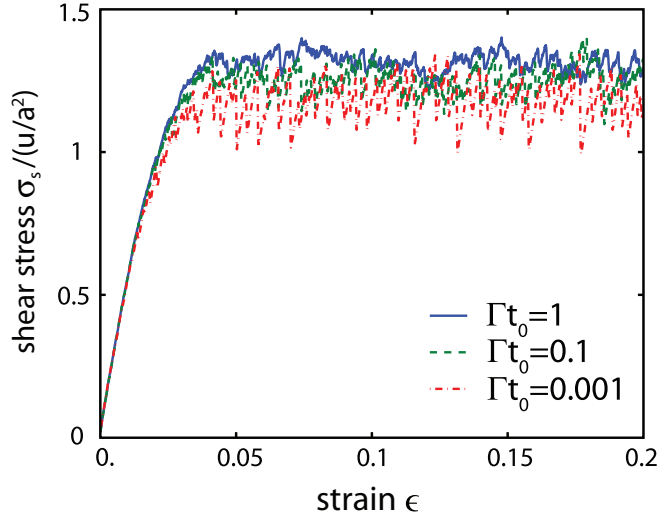
FIG. 2. (Color online) Typical stress-strain curves in two dimensions for system size $L = 219a$ and three different damping rates: $\Gamma t_0 = 1$ (solid blue line), $\Gamma t_0 = 0.1$ (dashed green line), and $\Gamma t_0 = 0.001$ (dash-dotted red line).

not only computationally expensive, but unnecessary. Even for our largest system sizes the time for sound waves to propagate across the system, $t_{\mathrm{prop}} = L/c \approx 250t_0$, is much smaller. Underdamped systems seldom show signs of further instability, such as kinetic energy spikes or stress drops, after about $2t_{\mathrm{prop}}–3t_{\mathrm{prop}}$.

In order to expedite draining the system of kinetic energy when $\Gamma t_0 = 10^{-3}$, we quench the kinetic energy rapidly by increasing Γ to $10t_0^{-1}$ once a threshold has been reached. Our criterion is that when the kinetic energy in the system has fallen to about 10^{-3} times the peak kinetic energy, the avalanche is effectively over and no other instabilities will be activated. For the viscous damping force discussed above, this is equivalent to a time criterion since the decay of the kinetic energy in the system is exponential. For comparison, the time for this decrease in kinetic energy is still roughly ten times larger than the time scale for sound to propagate across the largest simulation cell ($L = 875a$). It is also much larger than the time for the stress to reach its steady-state value (Fig. 1), indicating an event is over.

In order to verify that the quench procedure does not affect system evolution, we compared it to simulations with constant damping. For a subset of avalanches simulated with both the "quench" protocol and fixed damping rate, the total energy dissipated in each event differed by less than $10^{-9}u$. This is orders of magnitude smaller than the smallest avalanches recorded, which have energy $E \approx 10^{-5}u$. We conclude that the quench protocol produces a system in the same local potential energy minimum as the unquenched simulation.

Typical two-dimensional (2D) stress-strain loading curves are shown in Fig. 2. Curves for three-dimensional systems are similar. For all damping rates the systems reach steady state after roughly 5% strain. There is a small drift in the hydrostatic pressure at larger strains, but quantities of interest such as the shear stress and avalanche statistics become stationary and do not evolve with strain. Only avalanches at strains greater than 7% are included below.

Generically, the elastic energy density stored in a system by a differential strain $d\epsilon$ is $du_{\mathrm{strain}} = \sigma_{ij}d\epsilon_{ij}$, where σ_{ij} is the stress tensor and summation over repeated indices is implied. Because the 2D strain geometry is pure shear, this can be simplified by defining $\epsilon \equiv \epsilon_{xx} = -\epsilon_{yy}$ and $\sigma_s \equiv \sigma_{xx} - \sigma_{yy}$. The stored elastic energy density is then

$$du_{\mathrm{strain}} = \sigma_s d\epsilon. \tag{3}$$

The elastic strain energy in three dimensions has the same form if one defines $\sigma_s \equiv \sigma_{xx} + \sigma_{yy} - 2\sigma_{zz}$ and $\epsilon \equiv \epsilon_{xx} = \epsilon_{yy} = -1/2\epsilon_{zz}$.

III. RESULTS

A. Time dependence of stress and energy

This section illustrates some of the dramatic effects that inertia has on the mean of and fluctuations in the shear stress and potential energy density in steady-state quasistatic shear. One limiting case is the overdamped (large-Γ) regime, where the potential energy decreases monotonically to the next minimum during each avalanche. In the opposite, underdamped limit, there is negligible damping during plastic rearrangement and inertia can carry the system over successive small energy barriers. We present typical results from these limiting regimes with damping rates $\Gamma t_0 = 1$ and 0.001, respectively. Reference [47] identified a critical intermediate damping rate of $\Gamma t_0 = 0.1$ that acts like a multicritical point separating the overdamped and underdamped regimes. We find that this crossover damping rate is the same in two and three dimensions within our uncertainty.

Figure 3 illustrates how damping affects the potential energy density and stress. Note that systems with different damping rates sample completely different regions of phase space with almost no overlap. Differences of approximately 30% in the mean value of the potential energy density persist in our largest system sizes in two dimensions. There is a smaller but significant change of about 10% in the mean stress. In three dimensions the mean potential energy in the overdamped and underdamped limits differs by about 8% and the stress by 6%. As the damping decreases, inertia is able to carry the system over barriers in the potential energy landscape to progressively lower minima. In addition to reducing the mean potential energy, inertia leads to larger avalanches. The increase in the size of energy and stress drops is evident in Fig. 3 and related to changes in scaling exponents discussed below.

As illustrated in Fig. 3, the evolution of the stress and potential energy density is characterized by linear rises, where elastic energy is stored, and sudden drops during avalanches. Each avalanche can be characterized by the potential energy density drop $\Delta\mathcal{U}$ and stress drop $\Delta\sigma_s$. In what follows we want to compare avalanches of the same absolute size in systems of different linear dimension L. We define absolute measures of energy and stress drop as

$$E \equiv L^d \Delta\mathcal{U}, \quad S \equiv \frac{\langle\sigma_s\rangle L^d}{4\mu}\Delta\sigma_s. \tag{4}$$

The shear modulus μ and the steady-state shear stress $\langle\sigma_s\rangle$ are introduced so that both S and E have units of energy. We have found that both μ and $\langle\sigma_s\rangle$ are nearly independent of system size and relatively insensitive to damping rate.
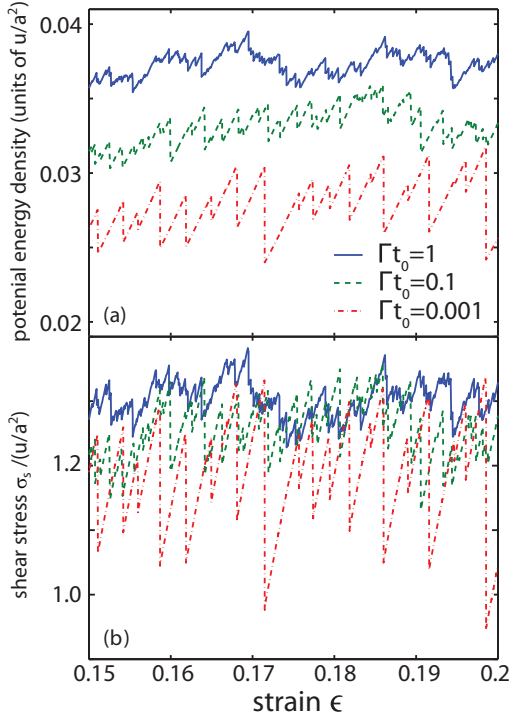
FIG. 3. (Color online) (a) Potential energy and (b) stress in three systems during a representative strain increment. The three systems of length $L = 219a$ started at the same zero-strain particle configuration but evolved with different representative damping rates: $\Gamma t_0 = 1$ (solid blue line), $\Gamma t_0 = 0.1$ (dashed green line), and $\Gamma t_0 = 0.001$ (dash-dotted red line). The mean values and the size and rate of fluctuations in energy and stress vary significantly with damping rate.

With these normalizations, energy conservation imposes a sum rule

$$\sum_i E^{(i)} = \sum_i S^{(i)}, \qquad (5)$$

where the sum is over all avalanches i in the steady-state regime. This connection has been noted previously by Lerner and Procaccia [45] and is derived in Appendix A.

The sum rule in Eq. (5) only constrains the sum over all events, but one might expect that something similar to the principle of detailed balance leads to a correlation between E and S for individual events. This correlation clearly breaks down for small events. Indeed, while E is always positive, S can have either sign for small events [45]. Large events dominate the sums in Eq. (5) and their energy and stress drops are more strongly correlated.

Figure 4 shows how the mean and variation in S for events of a given E change with avalanche size. Results are normalized by E to accentuate deviations from linear behavior and results from different damping rates are offset to prevent overlap. For energies less than a crossover energy the mean stress drop is much larger than E and has large fluctuations. In the overdamped regime this crossover occurs between $1u$ and $2u$ for both two and three dimensions, while for the crossover damping regime we estimate the crossover energy to occur between $2u$ and $4u$. The presence of large fluctuations and occasional negative drops suggests that events smaller than these crossovers do not necessarily contribute to a release of
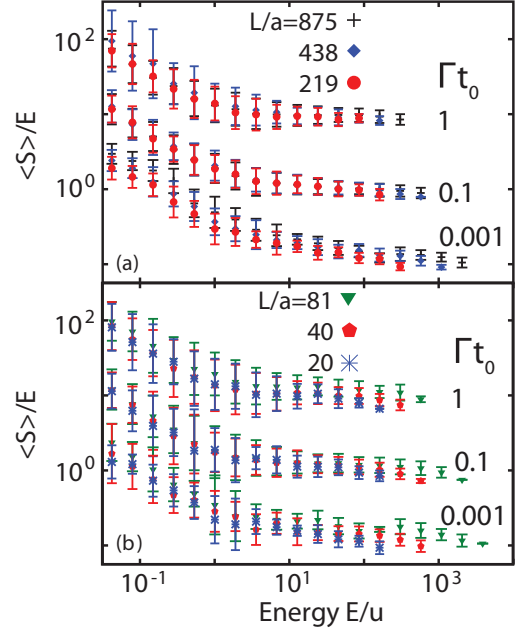

FIG. 4. (Color online) Ratio of mean stress drop to energy drop $\langle S \rangle / E$ of the avalanche events for (a) 2D and (b) 3D systems, binned by the logarithm of energy. To prevent overlap, the results for overdamped and underdamped systems are multiplied by 10 and 0.1, respectively. Error bars indicate the spread in stress drop for avalanches of a given energy. A linear relationship between $\langle S \rangle$ and E holds for E greater than a few u for the overdamped and crossover damping.

the imposed shear stress. For energies larger than the crossover energy the mean stress drop is nearly equal to E for the overdamped and crossover damping cases. Only these larger events exhibit critical scaling for both E and S. Figure 4 implies that E and S should have the same scaling exponents in this regime.

In the underdamped limit, $\langle S \rangle / E$ only approaches unity for the largest events, which move to larger E as L increases. The sum rule is not violated, but the scaling of avalanches with E and S may be different. The data can be fit to a power law $\langle S \rangle \sim E^{\eta}$ with $\eta \approx 0.9$ over the range $5u < E < 2000u$, but the prefactor must be L dependent so that $S/E \to 1$ at the largest events. The deviation from linearity is a natural result of reduced damping and inertia. In the overdamped limit there should be a correspondence between stress and potential energy, as traversing each potential energy barrier dissipates energy. In the underdamped limit potential energy barriers may be surmounted with little energy dissipation, leading to decoupling of the dissipated energy and the stress drop. The implications of this decoupling are discussed further in the section on finite-size scaling (Sec. III C).

B. Avalanche distributions

To characterize the different universality classes associated with the three damping regimes we examine the behavior of the avalanche rate distribution. To form this distribution we count the number of avalanche events with energy drop E or stress drop S during a given strain interval. We define the rate of events as the number of events per unit strain and energy.
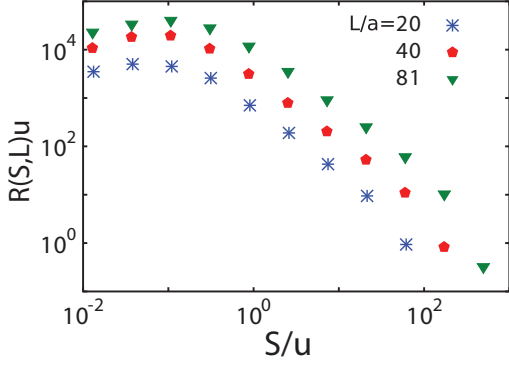
FIG. 5. (Color online) Unscaled distribution of stress drops $R(S,L)$ for overdamped 3D systems.

The rates of events with size E and S in a system of length L are denoted by $R(E,L)$ and $R(S,L)$, respectively.

Raw $R(S,L)$ distributions for the overdamped regime in three dimensions are shown in Fig. 5. As expected, the number of events of a given size increases with system size. One might expect the rate of small avalanches $R(S,L)$ to scale with the number of particles, i.e., as L^d. This would be the case if the density of nucleation sites were independent of system size. Many previous studies of avalanche behavior, for example, in interface depinning, have found or assumed this extensive scaling [8,50,51]. In contrast, we find subextensive scaling in the avalanche rate distribution for all damping rates in both two and three dimensions.

Figure 6 shows $R(S,L)$ and $R(E,L)$ scaled by L^γ with γ chosen to collapse the distributions for E and S within the critical scaling range. Results for two and three dimensions are similar and only one example is shown for each Γ. For different geometries and damping rates both $R(S,L)$ and $R(E,L)$ follow a power-law dependence on avalanche size from $\sim u$ up to a maximum size that grows with system size. Note that the nature of the cutoff at large avalanche sizes varies with damping rate. There is a simple rapid decay in the number of large events for the overdamped and crossover cases. For the underdamped case there is an excess of large events that leads to a plateau before the distribution cuts off.

We have already shown in Fig. 4 that E and S become decorrelated for energy drops smaller than a crossover energy. The distributions $R(S,L)$ and $R(E,L)$ also differ below this scale and only follow critical scaling for larger events. For underdamped systems, $R(E,L)$ and $R(S,L)$ both show L-dependent saturation below $E \sim 0.3u$ and $S \sim 2u$, respectively. For overdamped and crossover systems $R(S,L)$ saturates for $S \lesssim 0.1$ while $R(E,L)$ continues to rise as a power law as E decreases. At the crossover damping, $R(E,L)$ follows a single power law up to the size-dependent cutoff. For overdamped systems there is a change in power law at $E \sim u$. The exponent for small avalanches is less than unity and varies with system size. Previous simulations [42–44] have also observed this regime, but were too small ($L \lesssim 50a$) to see the critical scaling at large E. Note that $L = 55a$ results are cut off by system size at $E \gtrsim 8u$, giving less than a decade of scaling.

Table I lists the values of γ that give the best collapse of $R(E,L)$ and $R(S,L)$ in the critical scaling region from
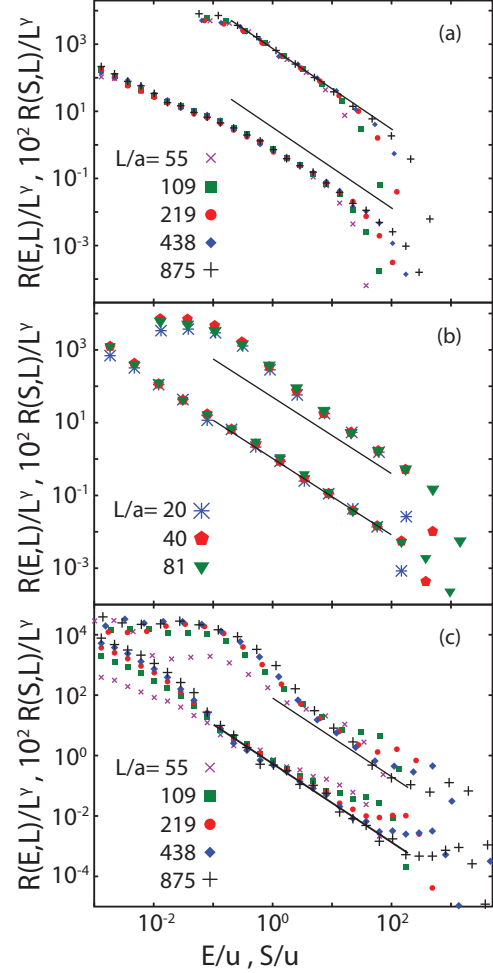

FIG. 6. (Color online) Avalanche distributions $R(S,L)$ and $R(E,L)$ scaled by L^γ for the (a) 2D overdamped ($\Gamma t_0 = 1$), (b) 3D crossover ($\Gamma t_0 = 0.1$), and (c) 2D underdamped ($\Gamma t_0 = 0.001$) regimes. In each panel, $R(S,L)$ is multiplied by a factor of 100 to prevent overlap. Straight lines indicate power laws with the exponents τ given in Table I.

the crossover energy to the upper cutoff. Quoted uncertainties indicate where deviations between curves for different L differ by more than the statistical errors, which are comparable to the symbol size. As noted above, γ is substantially less than d in all cases. One possible origin of the subextensive scaling ($\gamma < d$) is that the same local nucleation site is likely to produce a bigger avalanche in larger systems because there are more surrounding regions to trigger. Another is tied to the growth in the size of the largest events with L. These larger avalanches may reduce the probability that a given region can nucleate small events. The size of the largest avalanches increases with decreasing Γ and there is a corresponding drop in γ.

Note that for the overdamped regime the stress distribution shows a larger range of power-law scaling in Fig. 6, while in the crossover and underdamped regimes the energy drop shows a larger range of power-law behavior. The deviation in behavior of S and E comes from the regions where $\langle S \rangle / E > 1$ in Fig. 4. This region extends to larger E as L increases for underdamped systems. There is a corresponding shift to larger S in the start of the scaling regime in $R(S,L)/L^\gamma$.

TABLE I. Scaling exponents determined for overdamped ($\Gamma t_0 = 1$) and underdamped ($\Gamma t_0 = 0.001$) limits and at the crossover regime $\Gamma t_0 = 0.1$ in two and three dimensions. Quoted values satisfy the scaling relation $\gamma = d - (2 - \tau)\alpha$ and error bars are estimated from the finite-size-scaling collapses for E and S. The probability of avalanches decays as $E^{-\tau}$, the largest avalanche scales as L^{α}, the rate of small avalanches scales as L^{γ}, and the range of stresses scales as $L^{-\phi}$.

Γ	d	τ	α	γ	ϕ
1.0	2	1.3 ± 0.1	0.9 ± 0.05	1.3 ± 0.1	1.00 ± 0.1
0.1	2	1.0 ± 0.05	0.8 ± 0.1	1.2 ± 0.1	0.9 ± 0.1
0.001	2	1.25 ± 0.1	1.6 ± 0.1	0.8 ± 0.1	0.5 ± 0.1
1.0	3	1.3 ± 0.1	1.1 ± 0.1	2.1 ± 0.1	1.5 ± 0.2
0.1	3	1.05 ± 0.05	1.5 ± 0.1	1.6 ± 0.1	1.30 ± 0.1
0.001	3	1.2 ± 0.1	2.1 ± 0.2	1.3 ± 0.2	0.9 ± 0.1

Given the above observations, the most accurate exponents are obtained from $R(S,L)$ in overdamped systems and $R(E,L)$ for crossover and underdamped systems. The difference is only significant for the underdamped case. In fact, the value of γ recorded for the underdamped regime is substantially different from the previously reported value of 1.2 in Ref. [47]. This is because previous analysis had regarded the collapse of $R(S,L)$ with more importance and had considered small events ($S < u$) in the fit. The current collapse puts more emphasis on the quantity $R(E,L)$ and only attempts to collapse the scaling region $E > u$.

The solid lines in Fig. 6 show power-law fits $R(\chi,L) \sim \chi^{-\tau}$ with τ given in Table I and $\chi = S$ for overdamped systems and $\chi = E$ for other cases. Parallel lines are drawn near $R(E,L)$ for overdamped systems and $R(S,L)$ for other cases. The results are clearly consistent with power-law scaling over three decades in event size, but the precise limits of the critical region where the slope of the distributions should be fit are difficult to determine using this figure. As in other critical systems, finite-size scaling of results for different L provides a better method for determining the range of critical scaling for the avalanche rate distribution [52,53].

C. Finite-size scaling

The assumption underlying the finite-size-scaling procedure is that rather than depending separately on S or E and L, the avalanche rate distributions are a function only of the ratio of avalanche size to a power of the system size [52]. They then obey the scaling ansatz

$$R(\chi,L) = L^{\beta}g(\chi/L^{\alpha}), \tag{6}$$

where χ is either E or S and $g(x)$ is a scaling function that depends on damping rate Γ and may be different for E and S. The scaling function decays to zero at large arguments so that there are few avalanches above a largest size $\chi_{\max}$ that increases with system size as L^{α}. Given the assumption that no smaller energy or length scales are important, $g(x)$ must scale as a power law at small arguments:

$$g(x) \sim x^{-\tau}, \quad x \ll 1. \tag{7}$$

As shown above, the number of avalanches of a given size χ scales as L^{γ} for $\chi < \chi_{\max}$. Combining Eqs. (6) and (7) gives

$$R(\chi,L) = L^{\beta}g(\chi/L^{\alpha}) \sim L^{\beta+\alpha\tau}\chi^{-\tau}. \tag{8}$$

This gives us our first scaling relation between exponents

$$\gamma = \beta + \alpha\tau. \tag{9}$$

Another scaling relation can be derived from energy balance in steady state. The total work per unit volume per unit strain is just the mean stress $\langle\sigma_s\rangle$. Equating the total work done in the entire system to the sum of energy drops in all avalanches one finds

$$\int R(E,L)E\,dE = \langle\sigma_s\rangle L^d. \tag{10}$$

Inserting the scaling relation and changing variables to $x = E/L^{\alpha}$, one finds

$$L^{\beta+2\alpha}\int g(x)x\,dx \sim L^d, \tag{11}$$

yielding

$$\beta = d - 2\alpha. \tag{12}$$

Note that the integral in Eq. (11) converges and is insensitive to the lower bound because $\tau < 2$ for all systems. If hyperscaling was obeyed, $\gamma = d$ would imply $\tau = 2$, which is clearly inconsistent with the data.

Figure 7 shows finite-size-scaling collapses for both the energy and stress drop using the scaling ansatz in Eq. (6), with β obeying Eq. (12). The exponent α is chosen so that data for large events from different system sizes collapse onto a universal curve that corresponds to the scaling function $g(\chi/L^{\alpha})$. In all cases the curves deviate from the scaling function at a scaled energy $E \sim u/L^{\alpha}$, which decreases with increasing L. The energy of a single bond ($\sim u$) is a natural discrete energy scale where the assumption of scale invariance underlying Eq. (6) breaks down. We also considered collapses where β was allowed to deviate from the scaling relation in Eq. (12), but found there was no significant improvement. As with the exponent γ, the uncertainties in the value of α are determined by varying α and finding a range of values over which the collapse is acceptable. This determination utilizes the fact that the symbol sizes in Fig. 7 are comparable to the error bars.

The exponent τ listed in Table I is found by multiplying the distributions $R(\chi,L)$ by χ^{τ} in order to make the curves flat over the range of energies from u to $\chi_{\max}$ (figures not shown). The uncertainty in the exponent τ is determined from the range of values over which the distributions appear approximately flat. The values of the exponent τ given in Table I are consistent with the scaling relation (9) and fit the unscaled data shown in Fig. 6. In the overdamped regime fits to $R(S,L)$ give the smallest uncertainty and in the other cases fits to $R(E,L)$ extend over the longest range. Fits to S and E only differ significantly for the underdamped case. The slope of $R(E,L)$ is given in Table I, while the slope of $R(S,L)$ appears larger for both two and three dimensions, closer to $\tau \approx 1.5$ for certain energy ranges. This difference in slope can be explained by the features in Fig. 4. Since S and E are not linearly related, their distributions should also differ slightly, with $R(S,L)$ being
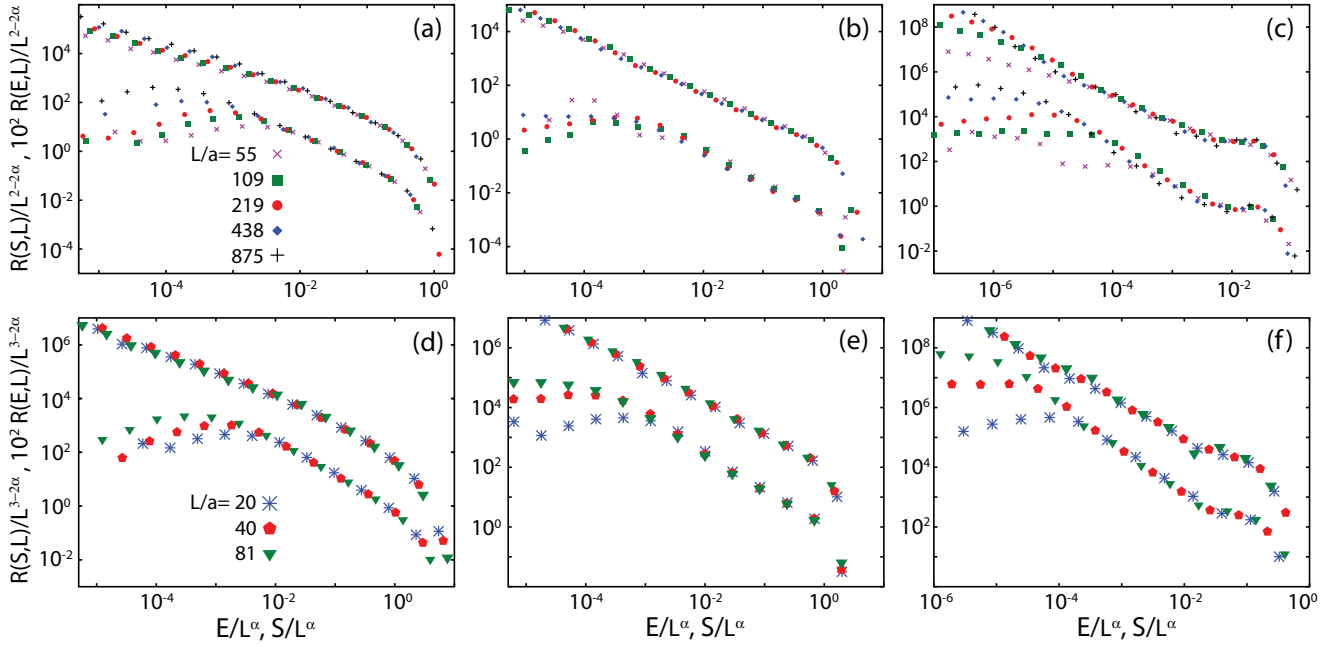
FIG. 7. (Color online) Finite-size scaling collapse for $R(E,L)$ and $R(S,L)$ distributions in two dimensions (top) and three dimensions (bottom) for (a) and (d) overdamped, (b) and (e) crossover, and (c) and (f) underdamped regimes. The value of α used in each collapse is given in Table I and symbol sizes are comparable to statistical error bars.

steeper. As with the exponent γ, our previous paper [47] reported a larger value for τ. This steeper slope reflects a value consistent with the distribution $R(S,L)$ as opposed to $R(E,L)$.

It is clear from the finite-size-scaling collapses that dimensionality does not affect the function $g(x)$, but that its form changes with damping rate. The form of $g(x)$ in the underdamped regime is of particular interest. It displays a characteristic plateau at large avalanche sizes in both two and three dimensions. Such an excess of large avalanches is seen in both earthquakes and experiments on sand [7,26,38]. An excess of system spanning events has also been seen in the Burridge-Knopoff model. In some versions of that model a consistent finite-size-scaling collapse was not found because a high-energy peak separated from the lower part of the distribution [54–56]. In our system there is a plateau rather than a second peak and the entire distribution collapses at large scaled energies.

D. Spatial extent of avalanches

The goal of this section is to relate the spatial extent of the plastic deformation produced by avalanches to the corresponding energy and stress drops. This is complicated by the long range of elastic interactions. The simplest type of shear displacement involving a local rearrangement of a few atoms produces elastic strains that decay as r^{-d}, where r is the distance from the atoms and d the dimension [57–60]. A threshold must be introduced to distinguish these small elastic strains from the plastic deformations in the central region. Appendix B describes how deviations from the power-law decay of strain fields can be used to determine the threshold used in this section. Note that this threshold changes

quantitative prefactors in the following discussion, but does not affect any of the general conclusions.

To define strain fields we first find the displacement of each atom during an avalanche. Previous work has emphasized the importance of subtracting any affine component of these displacements that reflects deformation of the box [60–62], but this contribution vanishes in our simulation because no strain is imposed during the avalanche. The derivative of the displacement field is calculated by taking a finite difference of displacements on nearby atoms. In two dimensions we form a Delaunay triangulation of the particle positions. A linear fit to the displacements of the particles on the corners of each triangle gives $\partial u_i/\partial x_j$, the derivative of the displacement **u** along direction i with respect to x_j [63]. The symmetrized strain tensor $\epsilon_{ij} = 1/2(\partial u_i/\partial x_j + \partial u_j/\partial x_i)$ is then constructed to eliminate the effect of any translation or rotation of the triangle. In three dimensions, the strain is obtained from finite differences on a tetrahedral tiling.

The magnitude of the strain is usually quantified by rotational invariants. The first, the trace of the strain tensor, measures the magnitude of dilational strains. Shear is most simply related to the second deviatoric strain invariant J_2. We define

$$\epsilon_d \equiv \sqrt{J_2} = \sqrt{\tfrac{1}{2}\mathrm{Tr}\big(\overset{\leftrightarrow}{\epsilon}{}^2_{\mathrm{dev}}\big)}, \tag{13}$$

where $\overset{\leftrightarrow}{\epsilon}_{\mathrm{dev}} \equiv \overset{\leftrightarrow}{\epsilon} - d^{-1}\mathrm{Tr}(\overset{\leftrightarrow}{\epsilon})\,\overset{\leftrightarrow}{I}$ is the deviatoric strain tensor. In the case of a simple shear strain ϵ_s in the x-y plane, then $\epsilon_s = \epsilon_d$. Triangles or tetrahedra with ϵ_d greater than a threshold value ϵ_c are identified as plastic. Based on the results of Appendix B, we use $\epsilon_c = 0.22$ in both two and three dimensions. This is comparable to the ideal elastic limit
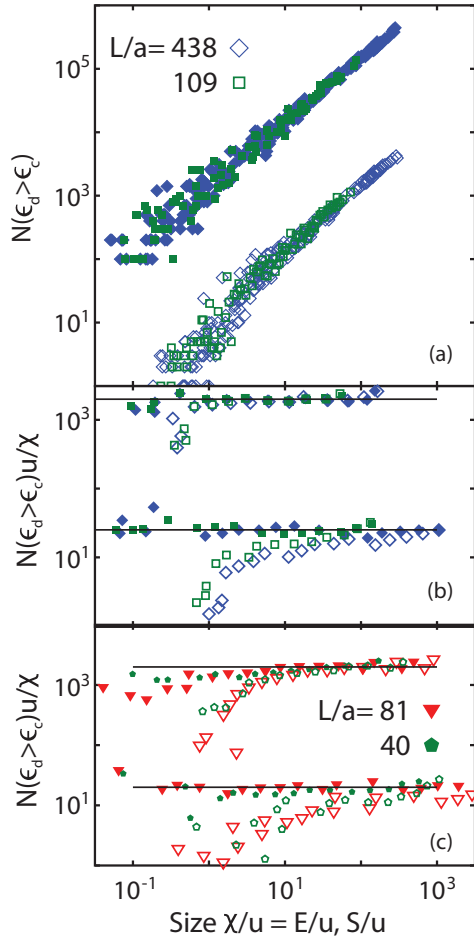
FIG. 8. (Color online) (a) Number of plastically deformed Delaunay triangles ($\epsilon_d > 0.22$) during a plastic event versus stress drop S (open symbols) and energy drop E (closed symbols) for two-dimensional systems of the indicated size at crossover damping. Data for E have been multiplied by 100 to prevent overlap. (b) Ratio of number of triangles to mean event size χ with $\chi = E$ (closed symbols) and $\chi = S$ (open symbols) for $\Gamma t_0 = 0.001$ and 1. (c) Ratio of number of plastically deformed tetrahedra to χ for 3D systems of the indicated size at $\Gamma t_0 = 0.001$ and 1. Results for $\Gamma t_0 = 1$ in (b) and (c) are multiplied by 100 to prevent overlap.

in dislocation-free crystals. Similar results are obtained with other thresholds and by using the dilational strain.

Figure 8(a) shows plots of the number of plastically deformed triangles $N(\epsilon_d > \epsilon_c)$ vs event size for $\Gamma t_0 = 0.1$. The data for energy drop E (open symbols) have been multiplied by 100. Events in the scaling range ($S, E > u$) show a linear relation between the event size (S or E) and area of the plastic deformation. Data for $\Gamma t_0 = 1$ and 0.001 are similar.

It is not obvious that the spatial extent and energy of events must be proportional. In particular, larger events could be associated with greater dissipation in each spatial region rather than a spread to new regions. To test this we found the average E or S of events with a given spatial size. Figure 8(b) shows the ratio of spatial size to mean energy in the overdamped and underdamped limits. Results for different Γ are offset to avoid overlap. For the overdamped data the

spatial size of systems is proportional to both E and S for events in the scaling region identified in previous sections ($S > 2u$ and $E > 0.3u$). The energy and spatial size are also proportional for the underdamped case. In contrast, results for S only asymptotically approach a linear relation for the largest events, which grow in size as L increases. This deviation is further evidence that E is the most natural quantity for the finite-size-scaling collapses of underdamped systems.

The straight lines drawn in Fig. 8(b) are the best fit for the number of plastically deformed triangles per unit energy. The values are about $20u^{-1}$ for the underdamped systems and $18u^{-1}$ for the overdamped systems. The constant energy dissipation per unit area is consistent with limited local plasticity and local particle displacements during avalanche events. Such behavior was found in previous 2D simulations, where the total nonaffine displacement of particles over strain intervals of $1/L$ was at most a [63]. Displacements by a single-particle diameter are sufficient to completely change the local forces and thus the shear stress driving further deformation.

Figure 8(c) shows that the plastically deformed volume also scales linearly with event energy in three dimensions. As in two dimensions, the stress drop in underdamped systems is less simply related to the plastic volume. The horizontal lines in Fig. 8(c) indicate that the number of plastic tetrahedra per unit dissipated energy is about $20u^{-1}$ for all damping rates. This result and the corresponding value for two dimensions explain the limit of the scaling region to energies of order $0.1u$ and above. At $0.1u$ there are only a handful of triangles or tetrahedra that deform plastically. It is natural that the finite-size-scaling ansatz breaks down and the discreteness of the system becomes important when events involve only a few particles.

Given the linear relation between energy and the total size of the plastically deformed region, the largest events involve $\sim L^\alpha$ triangles or tetrahedra. This implies that α is an effective fractal dimension. Typical examples of large avalanches are shown in Fig. 9. In the overdamped limit avalanches contain a number of disconnected regions that tend to lie along diagonal lines. While the disconnected regions span the system, they are separated by larger gaps and thus the fractal dimension is less than unity. In the underdamped limit, $\alpha > d - 1$ and the deformed region spreads across the system with only small breaks. The clusters are still highly directional with correlations along the diagonals that have been discussed in past studies of continuous and lattice models [21,24]. These striking changes in avalanche geometry with Γ represent another qualitative difference between underdamped and overdamped systems that may be readily accessible to experiments.

E. Distribution of stress values

One of the most basic quantities measured in a deformation simulation or experiment is the stress. In this section we consider the distribution of shear stress values before and after each event $P(\sigma_s)$. Figure 10 shows the distribution of stress values before (closed symbols) and after (open symbols) avalanches for 2D underdamped systems of different size. The distributions narrow about a limiting mean value as the system
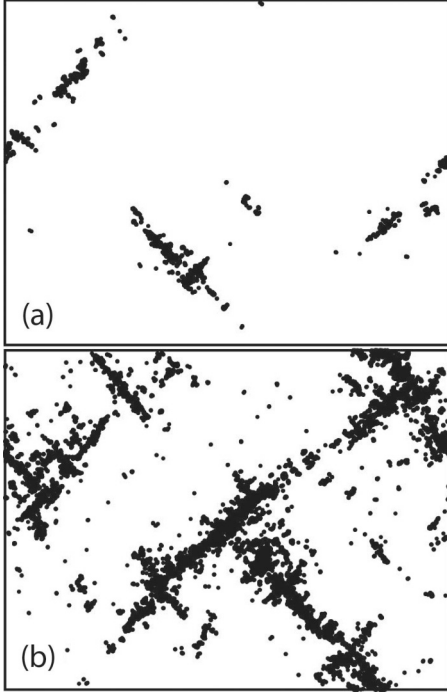
FIG. 9. Spatial distribution of plastically deformed triangles in examples of the largest events in (a) overdamped and (b) underdamped systems with $L = 875a$. The overdamped avalanches have gaps that are large compared to the plastic regions, while the overdamped avalanche spans the system with only small gaps. Both show strong anisotropy.

size increases. If inertia drove the system away from criticality and the onset of shear was a first-order transition with hysteresis, one would expect a gap between the distribution of stresses before and after avalanches. There is no evidence of this separation in our results. Even as they narrow, the distributions of stresses before and after avalanches continue to overlap. For all cases considered, the shift between the two distributions is much smaller than their width. In the following we combine the two distributions to improve our statistics. The distribution of all instantaneous values of stress gives similar results.
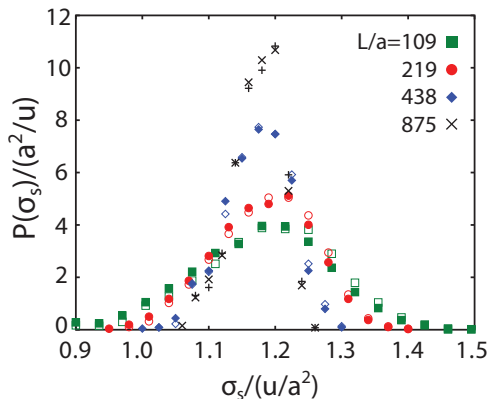

FIG. 10. (Color online) Probability distribution for stress values $P(\sigma_s)$ before (closed symbols and ×) and after (open symbols and +) each avalanche event in the two-dimensional system in the underdamped regime.

One way to describe the variation in $P(\sigma)$ with system size is to use a finite-size-scaling ansatz similar to Eq. (6) above. The shear stress distribution $P(\sigma_s)$ can be rewritten with a scaling function $h(x)$ as

$$P(\sigma_s) = L^\phi h(\tilde{\sigma}_s L^\phi), \tag{14}$$

where $\tilde{\sigma}_s = \sigma_s - \langle\sigma_s\rangle_L$ is the stress value with the system-size-dependent mean stress $\langle\sigma_s\rangle_L$ subtracted. The width of the distribution around the mean decreases as $L^{-\phi}$ with increasing L. Note that L must enter with the same power inside and outside the scaling function in order to preserve the normalization of the probability distribution.

We confirm the scaling form for the shear stress probability distributions given in Eq. (14) by finding values of ϕ that collapse results for the various system sizes and damping rates. Three such collapses are plotted in Fig. 11, while the best-fit values of ϕ for all systems simulated are listed in Table I.

Two upper bounds on the value of ϕ may be set. If there were an incoherent addition of stress from different regions with no correlations in time or space, one would expect the width of the distribution to scale as the inverse square root of the number of independent regions (or particles). This yields a relation $\sqrt{\langle(\sigma_s - \langle\sigma_s\rangle)^2\rangle} \sim L^{-d/2}$, or $\phi = d/2$. Correlations could make fluctuations decay more slowly with L so that $d/2$ is an upper bound for ϕ. The width of the distribution must also be at least as large as the stress change due to the largest avalanches, which are of order $L^{-(d-\alpha)}$. This implies that $\phi \leqslant d - \alpha$.

The values of ϕ listed in Table I satisfy the above bounds in all cases in two and three dimensions and ϕ is comparable to the smallest bound $\phi \approx \min(d/2, d - \alpha)$. The 2D overdamped and critically damped systems have $\phi \approx d/2 \approx d - \alpha$. In three dimensions it is clear that for the overdamped systems $d - \alpha$ is greater than the $d/2$ bound and $\phi \approx 1.5 = d/2$. Finally, in the underdamped regime $\alpha = 1.6$ in two dimensions and $\alpha = 2.1$ in three dimensions and in both cases $\phi \approx d - \alpha$. The crossover from $\alpha < d/2$ to $\alpha > d/2$ is equivalent to the crossover from positive to negative β, indicating that the rate of events of size $S_{max} \propto L^\alpha$ is decreasing, or the strain interval between such events is increasing. It appears that at this crossover, the events at L^α begin to dominate and set the width of the stress distribution.

The conclusion that the largest events can set the width of the stress distribution seems inconsistent with Fig. 10. There we found that the distributions of stresses before events and after events were nearly the same. The resolution of this discrepancy is that most events are small and can occur at any stage of the loading. The mean and standard deviation of the stresses before and after small events are indistinguishable from the global distribution.

For systems with $\alpha < d/2$ even the largest events have a similar distribution. This is evident in Fig. 3 for the overdamped case where the largest events are smaller than the spread in stress and occur at all stresses. For the underdamped case Fig. 3 is dominated by the large events that seem to have a characteristic scale and time interval. These large events are in the plateau region where the finite size of the system is important. While they remain the main source of fluctuations in stress for all L, the fractional change in shear stress goes
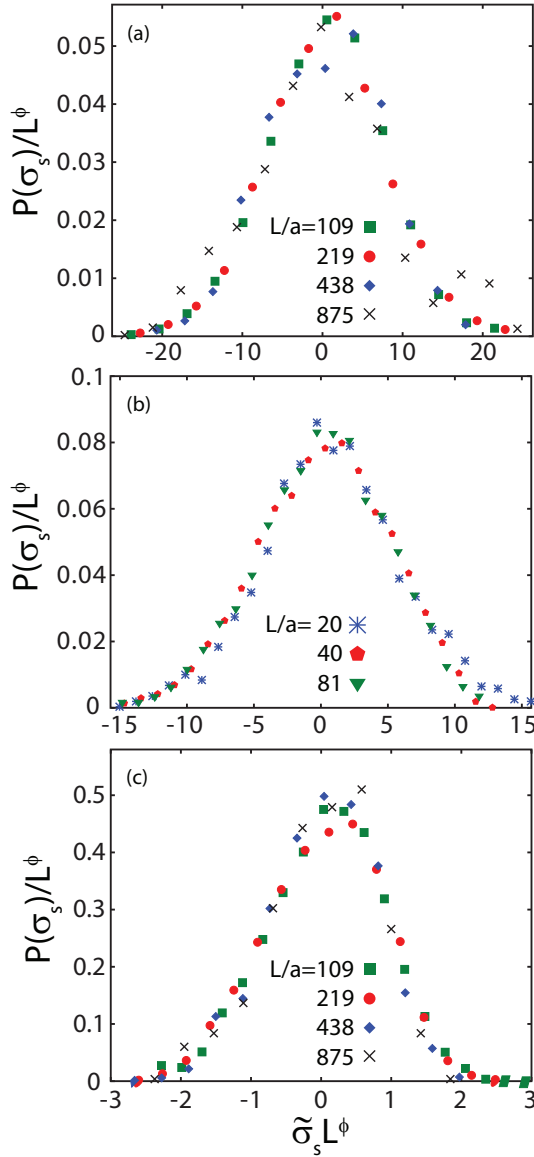
FIG. 11. (Color online) Scaled distribution of stress values $P(\sigma_s)$ before and after each avalanche event for the (a) overdamped system in two dimensions, (b) crossover damping in three dimensions, and (c) underdamped system in two dimensions. While the mean value is approximately constant for each damping rate, the distribution width scales with system size as $L^{-\phi}$. Values of ϕ are listed in Table I. Error bars are comparable to symbol size except for $L/a = 875$, where they are up to five times larger.

to zero as L increases because these largest events increase in size more slowly than L^d.

Studies of depinning often control the driving stress rather than the driving rate [10,17,50,64]. There is then a critical exponent ν relating the distance from the critical stress to the correlation length ξ, corresponding to the linear dimension of the largest avalanches: $\xi \sim |\sigma_c - \sigma|^{-\nu}$. While we have performed simulations with constant rate, the fact that the range of stresses scales as $L^{-\phi}$ suggests that $\nu = 1/\phi$. This relation applies in the limit where the largest avalanches set the range of stress fluctuations, giving $\nu = 1/\phi = 1/(d - \alpha)$. In the case where $\phi = d/2$, stress fluctuations are instead

set by uncorrelated fluctuations in the local properties of the system. As pointed out by Pázmándi *et al.* [65], $1/\phi$ does not correspond to the intrinsic ν for the correlation length in this case.

IV. SUMMARY AND DISCUSSION

In this paper we have presented a detailed analysis of the dramatic effects inertia has on quasistatic shear deformation of two- and three-dimensional disordered solids. During the intermittent avalanches of plastic activity, inertia can carry the system over successive energy barriers and thus change the ensemble of states sampled. The most direct evidence for this comes from measurements of the time-dependent potential energy density and shear stress (i.e., Fig. 3). Damping changes the mean energy density by about 30% in two dimensions and 8% in three dimensions, while the shear stress varies by 8% in two dimensions and 6% in three dimensions. Even for relatively small systems, e.g., $L = 200$ in two dimensions and 40 in three dimensions, there is no overlap between the range of energy densities sampled in the underdamped and overdamped limits.

Previous studies of scalar lattice models with rules designed to mimic inertia had predicted profound changes in the nature of the depinning transition with increasing inertia [10,13–16]. All found that the onset of shear became hysteretic, with different stresses needed to initiate and stop motion. Hysteresis is also present in the recently identified avalanche oscillator transition [66]. Our simulations of continuous systems show no hysteresis. In all cases the range of shear stresses and energy densities sampled during quasistatic shear goes to zero with increasing system size. The depinning transition is always continuous and a power-law distribution of avalanches is observed even in the underdamped limit. However, the scaling exponents are different in underdamped and overdamped limits.

Avalanches were characterized by the total energy dissipated E and an extensive quantity S proportional to the stress drop, which is more easily measured in experiments. A sum rule based on conservation of energy requires that the sums over all avalanches of E and S are equal, but does not relate the two quantities for individual events. Indeed, E is always positive, while S can be negative in small systems [45]. At sufficiently high energies, E and S become correlated and exhibit the same critical scaling. For high damping this threshold is a fraction of a single-particle bond energy, but the correlation moves to higher energies in the underdamped limit. For smaller events, the distribution of energies (not stresses) can exhibit power-law scaling over several decades in E that is not related to the critical behavior of larger avalanches. Past simulations used smaller system sizes where these noncritical avalanches dominated the statistics, making it difficult to determine critical scaling exponents [44–46].

Finite-size-scaling relations for the rate of avalanches of a given size in a system of length L were developed and used to determine scaling exponents as a function of damping. As in our earlier 2D studies, we find three universality classes corresponding to overdamped and underdamped limits and something analogous to a multicritical point at a crossover damping that separates them. Table I summarizes the numerical results for the scaling exponents.

One surprising aspect of the results is that the rate of small events is not proportional to the system size. If the probability that a local region would nucleate a small event was independent of system size, then the rate of small events would grow as L^d. The observed rate grows as L^γ with γ significantly less than d. One possibility is that local configurations that would only produce a small avalanche in a small system can trigger a string of other instabilities in a larger system. The long-range power-law decay of elastic interactions makes it more likely that they can affect scaling exponents in this way. The size of the largest avalanches grows with system size and it is also possible that these largest avalanches lower the number of nucleation sites for small avalanches. The difference between d and γ for all damping regimes in two and three dimensions represents a violation of hyperscaling. To our knowledge, values of γ have not been reported for lattice models of plastic deformation because authors have considered normalized distributions rather than absolute rates [10,13–16]. Violations of hyperscaling have been observed in percolation models and the random field Ising model, but were associated with the number of system-spanning clusters rather than the rate of smaller avalanches [53,67–69].

The scaling exponent α reflects the growth of the largest avalanches with system size $E_{\max} \propto L^\alpha$. Values of α in all systems are found to be less than the spatial dimension d. In the overdamped limit α is slightly lower than unity in two dimensions and slightly larger than unity in three dimensions. Previous simulations of smaller overdamped systems (less than 20 000 particles) reported $\alpha = 1$ [44] or 0.74 [45] in two dimensions and about 1.5 in three dimensions [46], but with significant uncertainties and poor collapses at the largest energies. Lattice models of overdamped avalanches that include the tensorial nature of shear stress find $\alpha = 1$ [21,22]. This is quite close to our simulation results, while scalar models predict $\alpha = 2$ [14,70]. The large difference in predictions for α make it a useful quantity to measure in future experiments, but we know of no existing studies. As noted above, α is effectively a fractal dimension for the plastically deformed region, which is generally disconnected and strongly anisotropic [24,58].

The largest avalanches grow much more rapidly with system size in the underdamped limit: $\alpha = 1.6 \pm 0.1$ and 2.1 ± 0.2 in two and three dimensions, respectively. As a result, these large avalanches dominate the fluctuations in instantaneous stress values, which scale as $L^{-\phi}$ with $\phi = d - \alpha$. Plots of the evolution of stress with time are dominated by these large events. In the overdamped regime, $\phi = d/2$, indicating that fluctuations are dominated by uncorrelated variations in interactions and geometry as the configuration of particles evolves.

Studies of avalanche statistics in slowly driven systems have generally focused on the exponent τ that describes the decrease in event rate with event size $R(E) \sim E^{-\tau}$. Our simulations reveal similar values of $\tau \approx 1.25$ for both underdamped and overdamped limits in two and three dimensions. The crossover damping has a lower value of $\tau \approx 1$. Direct fits of power laws over at least three decades are consistent with exponents obtained from finite-size-scaling relations. The only discrepancy is for scaling of stress drops in the underdamped limit. In this case, the stress drop rises less rapidly than the energy up to the size of the largest avalanches. This may be

because inertia is more likely to carry the system past barriers that lead to a lowering in stress than energy. The result is an apparent τ of about 1.5 over a limited range of stress drops and a poorer finite-size-scaling collapse. The fact that S and E are different in the underdamped limit may have implications for experimental studies where stress or slip displacements are often more directly accessible than energy.

Lattice models of overdamped dynamics that treat strain as a scalar variable predict a universal value of $\tau = 3/2$ that is clearly inconsistent with our scaling relations. Studies of a model that includes the directional nature of stress transfer found $\tau \approx 1.25$ [21], which is consistent with our results $\tau = 1.3 \pm 0.1$. A recently posted paper on the same lattice model finds a slightly higher value of $\tau \approx 1.35$, which is also within our error bars [71]. Neither study used finite-size scaling to determine τ.

As noted above, scalar lattice models predict hysteresis in the underdamped limit. This is inconsistent with our results and it would be interesting to see if anisotropic lattice models also predict hysteresis. It may also be that the hysteresis in scalar lattice models reflects the fact that they impose a fixed discrete barrier drop from inertia and fixed discrete changes in local strain at each lattice site after rearrangements. The distributions are continuous in our simulations and the effect of inertia may depend on the size of local energy barriers or rearrangements.

A critical review of experimental results for τ is beyond the scope of this paper, but the wide range of reported values reflects systematic uncertainties in measuring avalanches and analyzing their statistics. In many cases experiments are not in the steady-state regime considered here, but collect avalanche statistics at small strains during the transition from the initial elastic response to yield (i.e., $\epsilon < 0.07$ in Fig. 2). We find that this initial region is sensitive to preparation and exclude it from our analysis. In most cases the range of avalanche sizes is only one to two decades. Uncertainties in the limits of the scaling regime due to finite system size, finite temperature [72], distance from the critical stress [10], and experimental noise lead to uncertainties that are greater than the difference between $\tau = 1.5$ and 1.25. The finite-size-scaling method used here eliminates such systematic effects, but is difficult to replicate in experiments.

Earthquake statistics cover the largest range of event sizes, but involve a wide range of phenomena that are not included in simple models like ours [38]. Just one example is the finite thickness ($\sim$10 km) of the active region of the crust. There is a transition in the effective dimension of earthquake displacements as the size of the slipping region grows past this scale [73,74]. Seismologists also treat successive displacements along different faults as separate events, even though there is evidence that they are causally connected. Our quasistatic simulations group together all plastic activity resulting from an initial instability even if the activity occurs in widely separated regions and is separated by long quiescent periods. These long quiescent periods do not occur in lattice models where changes in local strain are discrete. We are currently evaluating methods of separating our avalanches into separate events and initial results suggest the effective value of τ could increase in the overdamped limit where quiescent periods are more common.

Given the difficulties in determining precise values of τ, it becomes interesting to consider the qualitative difference in the scaling function g for overdamped and underdamped systems. Models and experiments on overdamped systems generally find a simple exponential cutoff for large events [44–46,75,76]. In contrast, studies of earthquakes statistics for single faults often find an excess of large system-spanning events that is similar to the plateau seen in our underdamped simulations. Plateaus of this type are also evident in experimental studies of steady shear in glass bead packs [7]. Future experiments that focus on the form of the scaling function and the fractal dimension α of the largest avalanches may provide the most sensitive means of detecting inertial effects and testing theoretical models.

ACKNOWLEDGMENTS

APPENDIX A: SUM RULE DERIVATION

The sum rule in Eq. (5) follows from energy conservation. Each avalanche event i is accompanied by a potential energy density drop $\Delta\mathcal{U}^{(i)}$ and shear stress drop $\Delta\sigma_s^{(i)}$. This dissipated energy must be balanced by the work done on the system during segments where the system loads elastically. For a strain segment $\Delta\epsilon^{(j)}$ the work done on the system is $\sigma_s\Delta\epsilon^{(j)}L^d$. The assumption that there is a well defined steady-state mean potential energy density allows us to equate the sum of the energy drops with the total work done

$$\sum_i \Delta\mathcal{U}^{(i)}L^d = \sum_j \sigma_s\Delta\epsilon^{(j)}L^d, \tag{A1}$$

where the sum on the left is over all energy drops and the sum on the right is over all elastic loading segments, which are equal in number.

As shown in Figs. 2, 10, and 11 there is also a well defined steady-state shear stress. Thus we can rewrite Eq. (A1) as

$$\sum_i \Delta\mathcal{U}^{(i)}L^d = \langle\sigma_s\rangle \sum_j \Delta\epsilon^{(j)}L^d, \tag{A2}$$

introducing corrections proportional to the square of stress fluctuations, which go to zero as $L^{-2\phi}$ in the thermodynamic limit (Table I). A steady-state shear stress also implies that the stress rises during elastic loading balance the stress drops during avalanches over long strain intervals. The stress rise over each elastic interval j can be written as $\mu\Delta\epsilon^{(j)}$, where μ is the shear modulus, so that

$$\sum_i \Delta\sigma_s^{(i)}L^d = \sum_j 4\mu\Delta\epsilon^{(j)}L^d. \tag{A3}$$

Other workers have found that above a length scale much smaller than our system sizes variations in the modulus μ between different elastic segments are small [77].

In the main text we measured extensive stress and energy drops $S \equiv \Delta\sigma_s\langle\sigma_s\rangle L^d/4\mu$ and $E = \Delta\mathcal{U}L^d$ in order to compare avalanches across different system sizes. Combining the

relations above with the definitions of S and E allows us to relate total stress and energy drops

$$\sum_i S^{(i)} = \sum_i E^{(i)}. \tag{A4}$$

Since the summations are over the same set of avalanche events this also implies that the mean values are equal $\langle S\rangle = \langle E\rangle$.

APPENDIX B: DISTINGUISHING PLASTIC AND ELASTIC REGIONS

As noted in the main text, the strain field around a local plastic region decays as a power of the distance r from the region [57,59,60,78]. The prefactor should be proportional to the magnitude of the plastic rearrangement, which we find scales as the stress drop. Since the spatial arrangements of plastic regions can be complicated, we consider instead the distribution of local strain values $N(\epsilon_d)$. From the scaling of the phase space with distance r, we have $r^{d-1}dr \sim N(\epsilon_d)d\epsilon_d$. Then the distribution of local strains scales as a power law in two and three dimensions

$$N(\epsilon_d) \sim S\epsilon_d^{-2}. \tag{B1}$$

The cumulative distribution function (CDF) $N(\epsilon_d > x)$ of strains larger than x scales as

$$N(\epsilon_d > x) \sim Sx^{-1}. \tag{B2}$$

Figure 12(a) shows $N(\epsilon_d > x)$ averaged over avalanche events of a given stress drop S. Events with damping rate $\Gamma t_0 = 1$ are shown and curves for other damping rates are
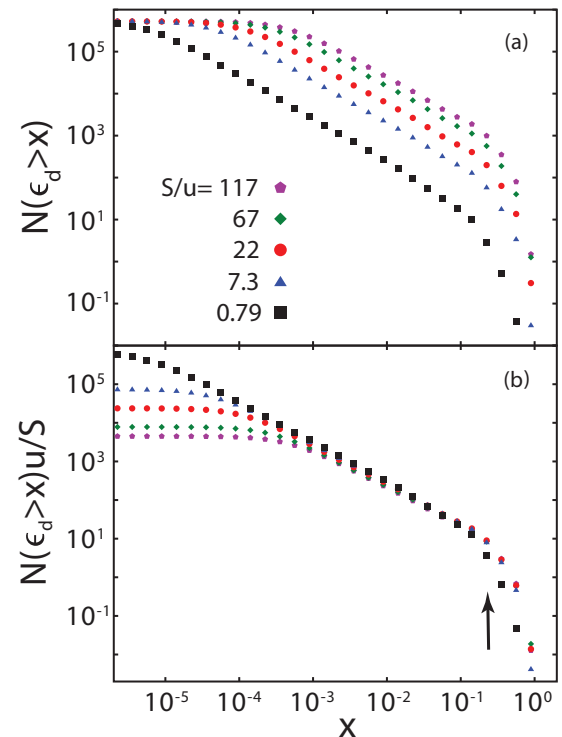

FIG. 12. (Color online) (a) The CDF of ϵ_d averaged over events of the indicated S in two dimensions for damping $\Gamma t_0 = 1$ and system size $L = 438a$. (b) The CDF after rescaling by S to collapse the elastic region. An arrow indicates $\epsilon_c = 0.22$.
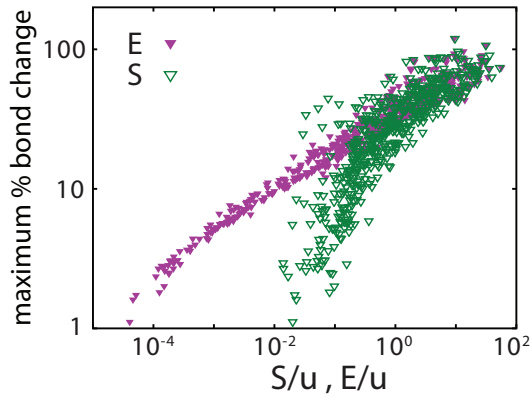
FIG. 13. (Color online) Maximum percentage bond change that occurs during an avalanche of stress drop S (open symbols) or energy drop E (closed symbols) in overdamped 2D systems with $L = 109a$. Similar results are obtained for other L and Γ.

similar. Above a minimum strain that grows with S, each curve follows the power-law scaling predicted by Eq. (B2). Equation (B2) also predicts that the prefactor of the power-law region should grow linearly with the size of the event. Figure 12(b) tests this prediction. We find that events large enough to be in the scaling regime ($S > u$) collapse onto a universal curve with a power-law regime that is cut off at strains bigger

than about $\epsilon_c = 0.22$. We associate this failure of the elastic prediction with the onset of plastic deformation in the main text. Note that smaller events are cut off at slightly smaller strains, providing further evidence that they involve different types of displacement.

Changes in bond length are another measure of local deformation that can be used to identify plastic regions. Figure 13 shows the maximum percentage change of any bond in the system as a function of event size. Note that there are almost no events where bonds change less than 2%. These are associated with extremely small events of order $E \sim 10^{-5}u$. For events in the scaling regime where S and E are comparable ($E > 0.3u$), the largest bond change is 20%. This is comparable to the displacements need to produce a local strain of ϵ_c.

Even the largest events produce only 100% bond changes, corresponding to displacements of the order of a bond length relative to neighbors. This is consistent with the conclusion in the main text that larger events produce a uniform amount of dissipation over larger regions rather than larger deformations in a fixed spatial region. The very slow increase in the maximum bond length change with event size for the largest events may be attributed to sampling more bond changes from a fixed distribution. This is consistent with the collapse of the CDF in Fig. 12.

[1] O. Perkovic, K. Dahmen, and J. P. Sethna, Phys. Rev. Lett. **75**, 4528 (1995).

[2] C. R. Myers and J. P. Sethna, Phys. Rev. B **47**, 11171 (1993).

[3] M. C. Miguel, A. Vespignani, S. Zapperi, J. Weiss, and J. R. Grasso, Nature (London) **410**, 667 (2001).

[4] S. Zapperi, C. Castellano, F. Colaiori, and G. Durin, Nat. Phys. **1**, 46 (2005).

[5] J. P. Sethna, K. A. Dahmen, and C. R. Myers, Nature (London) **410**, 242 (2001).

[6] P. Y. Chan, G. Tsekenis, J. Dantzig, K. A. Dahmen, and N. Goldenfeld, Phys. Rev. Lett. **105**, 015502 (2010).

[7] A. Baldassarri, F. Dalton, A. Petri, S. Zapperi, G. Pontuale, and L. Pietronero, Phys. Rev. Lett. **96**, 118002 (2006).

[8] N. Martys, M. O. Robbins, and M. Cieplak, Phys. Rev. B **44**, 12294 (1991).

[9] S. Zapperi, A. Vespignani, and H. E. Stanley, Nature (London) **388**, 658 (1997).

[10] N. Friedman, A. T. Jennings, G. Tsekenis, J.-Y. Kim, M. Tao, J. T. Uhl, J. R. Greer, and K. A. Dahmen, Phys. Rev. Lett. **109**, 095507 (2012).

[11] J. M. Schwarz and D. S. Fisher, Phys. Rev. E **67**, 021603 (2003).

[12] M. C. Marchetti, Pramana **64**, 1097 (2005).

[13] C. P. C. Prado and Z. Olami, Phys. Rev. A **45**, 665 (1992).

[14] K. A. Dahmen, Y. Ben-Zion, and J. T. Uhl, Phys. Rev. Lett. **102**, 175501 (2009).

[15] R. Maimon and J. M. Schwarz, Phys. Rev. Lett. **92**, 255502 (2004).

[16] K. Dahmen, Y. Ben-Zion, and J. T. Uhl, Nat. Phys. **7**, 554 (2011).

[17] M. J. Alava, P. K. V. V. Nukala, and S. Zapperi, Adv. Phys. **55**, 349 (2006).

[18] P. Cizeau, S. Zapperi, G. Durin, and H. E. Stanley, Phys. Rev. Lett. **79**, 4669 (1997).

[19] C. B. Picallo and J. M. López, Phys. Rev. E **77**, 046114 (2008).

[20] L. P. Kadanoff, S. R. Nagel, L. Wu, and S. M. Zhou, Phys. Rev. A **39**, 6524 (1989).

[21] M. Talamali, V. Petäjä, D. Vandembroucq, and S. Roux, Phys. Rev. E **84**, 016115 (2011).

[22] M. Zaiser and N. Nikitas, J. Stat. Mech. (2007) P04013.

[23] P. Bak, C. Tang, and K. Wiesenfeld, Phys. Rev. Lett. **59**, 381 (1987).

[24] C. E. Maloney and M. O. Robbins, Phys. Rev. Lett. **102**, 225502 (2009).

[25] J. M. Schwarz and D. S. Fisher, Phys. Rev. Lett. **87**, 096107 (2001).

[26] G. A. Held, D. H. Solina, D. T. Keane, W. J. Haag, P. M. Horn, and G. Grinstein, Phys. Rev. Lett. **65**, 1120 (1990).

[27] H. M. Jaeger, C. H. Liu, and S. R. Nagel, Phys. Rev. Lett. **62**, 40 (1989).

[28] P. Schall, D. A. Weitz, and F. Spaepen, Science (NY) **318**, 1895 (2007).

[29] B. Utter and R. P. Behringer, Phys. Rev. E **69**, 031308 (2004).

[30] B. Utter and R. P. Behringer, Phys. Rev. Lett. **100**, 208302 (2008).

[31] N. W. Hayman, L. Ducloué, K. L. Foco, and K. E. Daniels, Pure Appl. Geophys. **168**, 2239 (2011).

[32] B. Miller, C. O'Hern, and R. P. Behringer, Phys. Rev. Lett. **77**, 3110 (1996).

[33] F. Wu, Z. Zhang, J. Shen, and S. Mao, Acta Mater. **56**, 894 (2008).

[34] L.-Q. Xing, Y. Li, K. T. Ramesh, J. Li, and T. C. Hufnagel, Phys. Rev. B **64**, 180201 (2001).

[35] D. Jang, C. T. Gross, and J. R. Greer, Int. J. Plasticity **27**, 858 (2011).

[36] D. Jang and J. R. Greer, Nat. Mater. **9**, 215 (2010).

[37] M. Bretz, R. Zaretzki, S. B. Field, N. Mitarai, and F. Nori, Europhys. Lett. **74**, 1116 (2006).

[38] C. H. Scholz, *The Mechanics of Earthquakes and Faulting* (Cambridge University Press, Cambridge, 2002).

[39] R. Behringer (private communication).

[40] B. A. Sun, H. B. Yu, W. Jiao, H. Y. Bai, D. Q. Zhao, and W. H. Wang, Phys. Rev. Lett. **105**, 035501 (2010).

[41] B. Sun, S. Pauly, J. Tan, M. Stoica, W. Wang, U. Kühn, and J. Eckert, Acta Mater. **60**, 4160 (2012).

[42] S. Tewari, D. Schiemann, D. J. Durian, C. M. Knobler, S. A. Langer, and A. J. Liu, Phys. Rev. E **60**, 4385 (1999).

[43] D. J. Durian, Phys. Rev. E **55**, 1739 (1997).

[44] C. Maloney and A. Lemaître, Phys. Rev. Lett. **93**, 016001 (2004).

[45] E. Lerner and I. Procaccia, Phys. Rev. E **79**, 066109 (2009).

[46] N. P. Bailey, J. Schiøtz, A. Lemaître, and K. W. Jacobsen, Phys. Rev. Lett. **98**, 095501 (2007).

[47] K. M. Salerno, C. E. Maloney, and M. O. Robbins, Phys. Rev. Lett. **109**, 105703 (2012).

[48] S. Plimpton, J. Comput. Phys. **117**, 1 (1995).

[49] P. Allen and D. Tildesley, *Computer Simulation of Liquids* (Clarendon, Oxford, 1989).

[50] D. S. Fisher, Phys. Rep. **301**, 113 (1998).

[51] D. Stauffer and A. Aharony, *Introduction To Percolation Theory* (Taylor & Francis, London, 1994).

[52] V. Privman, *Finite Size Scaling and Numerical Simulation of Statistical Systems* (World Scientific, Singapore, 1990).

[53] O. Perković, K. A. Dahmen, and J. P. Sethna, Phys. Rev. B **59**, 6106 (1999).

[54] J. M. Carlson and J. S. Langer, Phys. Rev. Lett. **62**, 2632 (1989).

[55] J. M. Carlson, J. S. Langer, B. E. Shaw, and C. Tang, Phys. Rev. A **44**, 884 (1991).

[56] J. M. Carlson, Phys. Rev. A **44**, 6226 (1991).

[57] A. Lemaître and C. Caroli, Phys. Rev. Lett. **103**, 065501 (2009).

[58] C. E. Maloney and A. Lemaître, Phys. Rev. E **74**, 016118 (2006).

[59] G. Picard, A. Ajdari, F. Lequeux, and L. Bocquet, Eur. Phys. J. E **15**, 371 (2004).

[60] A. Tanguy, F. Leonforte, and J.-L. Barrat, Eur. Phys. J. E **20**, 355 (2006).

[61] C. Maloney and A. Lemaître, Phys. Rev. Lett. **93**, 195501 (2004).

[62] A. Lemaître and C. Caroli, Phys. Rev. E **76**, 036104 (2007).

[63] C. E. Maloney and M. O. Robbins, J. Phys.: Condens. Matter **20**, 244128 (2008).

[64] N. Martys, M. Cieplak, and M. O. Robbins, Phys. Rev. Lett. **66**, 1058 (1991).

[65] F. Pázmándi, R. T. Scalettar, and G. T. Zimányi, Phys. Rev. Lett. **79**, 5130 (1997).

[66] S. Papanikolaou, D. M. Dimiduk, W. Choi, J. P. Sethna, M. D. Uchic, C. F. Woodward, and S. Zapperi, Nature (London) **490**, 517 (2012).

[67] F. J. Pérez-Reche and E. Vives, Phys. Rev. B **67**, 134421 (2003).

[68] S. Fortunato, A. Aharony, A. Coniglio, and D. Stauffer, Phys. Rev. E **70**, 056116 (2004).

[69] K. Dahmen and J. P. Sethna, Phys. Rev. B **53**, 14872 (1996).

[70] D. S. Fisher, K. Dahmen, S. Ramanathan, and Y. Ben-Zion, Phys. Rev. Lett. **78**, 4885 (1997).

[71] Z. Budrikis and S. Zapperi, arXiv:1307.2135.

[72] H. G. E. Hentschel, S. Karmakar, E. Lerner, and I. Procaccia, Phys. Rev. Lett. **104**, 025501 (2010).

[73] J. F. Pacheco, C. H. Scholz, and L. R. Sykes, Nature (London) **355**, 71 (1992).

[74] B. E. Shaw, Bull. Seismol. Soc. Am. **99**, 871 (2009).

[75] E. Pratt and M. Dennin, Phys. Rev. E **67**, 051402 (2003).

[76] J. Lauridsen, M. Twardos, and M. Dennin, Phys. Rev. Lett. **89**, 098303 (2002).

[77] M. Tsamados, A. Tanguy, C. Goldenberg, and J.-L. Barrat, Phys. Rev. E **80**, 026112 (2009).

[78] C. E. Maloney, Phys. Rev. Lett. **97**, 035503 (2006).